

1 **Variability of vertical structure of precipitation with sea surface temperature over the**
2 **Arabian Sea and the Bay of Bengal as inferred by TRMM PR measurements**

3 **Kadiri Saikranthi¹, Basivi Radhakrishna², Thota Narayana Rao² and**

4 **Sreedharan Krishnakumari Satheesh³**

5 ¹ *Department of Earth and Climate Science, Indian Institute of Science Education and*
6 *Research (IISER), Tirupati, India.*

7 ² *National Atmospheric Research Laboratory, Department of Space, Govt. of India, Gadanki*
8 *- 517112, India.*

9 ³ *Divecha Centre for Climate Change, Centre for Atmospheric and Oceanic Sciences, Indian*
10 *Institute of Science, Bangalore - 560012, India.*

11

12

13

14

15

16

17

18

19

20

21

22

23

24

25

26

27

28

29

30 **Address of the corresponding author**

31 Dr. K. Saikranthi,

32 Department of Earth and Climate Science,

33 Indian Institute of Science Education and Research (IISER),

34 Tirupati,

35 Andhra Pradesh, India.

36 Email: ksaikranthi@gmail.com

37 **Abstract**

38 Tropical Rainfall Measuring Mission precipitation radar measurements are used to
39 examine the variation of vertical structure of precipitation with sea surface temperature (SST)
40 over the Arabian Sea (AS) and Bay of Bengal (BOB). The variation of reflectivity and
41 precipitation echo top with SST is remarkable over the AS but small over the BOB. The
42 reflectivity increases with SST (from 26°C to 31°C) by ~1 dBZ and 4 dBZ above and below
43 6 km, respectively, over the AS while, its variation is < 0.5 dBZ over the BOB. The
44 transition from shallow storms at lower SSTs ($\leq 27^\circ\text{C}$) to deeper storms at higher SSTs is
45 strongly associated with the decrease in stability and mid-tropospheric wind shear over the
46 AS. Contrary, the storms are deeper at all SSTs over the BOB due to weaker stability and
47 mid-tropospheric wind shear. At lower SSTs, the observed high aerosol optical depth (AOD)
48 and low total column water (TCW) over AS results in small cloud effective radius (CER) and
49 weaker reflectivity. As SST increases, AOD decreases and TCW increases leading to large
50 CER and high reflectivity. The changes in these parameters with SST are marginal over the
51 BOB and hence the CER and reflectivity. The predominance of collision-coalescence process
52 below the bright band is responsible for the observed negative slopes in the reflectivity over
53 both the seas. The observed variations in reflectivity are originated at the cloud formation
54 stage over both the seas and these variations are magnified during the descent of
55 hydrometeors to ground.

56

57

58

59

60

61

62

63 **1. Introduction**

64 Indian summer monsoon (ISM - June through September) is one of the most complex
65 weather phenomena, involving coupling between the atmosphere, land and ocean. At the
66 boundary of the ocean and atmosphere air-sea interactions play a key role for the coupled
67 Earth system (Wu and Kirtman 2005; Feng et al. 2018). The sea surface temperature (SST) –
68 precipitation relations are the important measures for the air-sea interactions on different
69 temporal scales (Woolnough et al., 2000; Rajendran et al. 2012). Recent studies (Wang et al.
70 2005; Rajeevan et al. 2012; Chaudhari et al. 2013; 2016; Weller et al. 2016; Feng et al. 2018)
71 have shown that the simulation of ISM can be improved with the exact representation of SST
72 - precipitation relationship. SST modulates the meteorological factors that influence the
73 formation and evolution of different kinds of precipitating systems over tropical oceans
74 (Gadgil et al. 1984; Schumacher and Houze, 2003; Takayabu et al. 2010; Oueslati and Bellon
75 2015).

76 The studies dealing with SST and cloud/precipitation population considered whole
77 Indian Ocean as a single entity (Gadgil et al. 1984; Woolnough et al., 2000; Rajendran et al.
78 2012; Sabin et al. 2012; Meenu et al. 2012; Nair and Rajeev 2014; Roxy 2014). But in reality
79 the Bay of Bengal (BOB) and the Arabian Sea (AS) of Indian Ocean possess distinctly
80 different features (Kumar et al. 2014; Shige et al. 2017; Rajendran et al. 2018; Saikranthi et
81 al. 2019). The monsoon experiment (MONEX) and Bay of Bengal monsoon experiment
82 (BOBMEX) have shown how these two seas are different with respect to each other, in terms
83 of SST, back ground atmosphere and the occurrence of precipitating systems (Krishnamurti
84 1985; Houze and Churchill 1987; Gadgil 2000; Bhat et al. 2001). The SST in the AS cools
85 between 10 °N and 20 °N during the monsoon season whereas warming is seen in other
86 global Oceans between the same latitudes (Krishnamurthi 1981). SST variability is large over
87 the AS than the BOB at seasonal and intraseasonal scales (Sengupta et al. 2001; Roxy et al.

88 2013). The monsoonal winds (in particular the low-level jet) are stronger over the AS than
89 BOB (Findlater 1969). Also, lower-tropospheric thermal inversions are more frequent and
90 stronger over the AS than BOB (Narayanan and Rao 1981; Sathiyamoorthy et al. 2013).
91 Thus, the atmospheric and sea surface conditions and in turn the occurrence of different kinds
92 of precipitating systems are quite different over the BOB and the AS during the ISM period.
93 For instance, long-term measurements of Tropical Rainfall Measuring Mission (TRMM)
94 precipitation radar (PR) have shown that shallow systems are more prevalent over the AS,
95 while deeper systems occur frequently over the BOB (Liu et al. 2007; Romatschke et al.
96 2010; Saikranthi et al. 2014, 2018; Houze et al. 2015).

97 The aforementioned studies mainly focused on the morphology of vertical structure of
98 precipitation, but, none of them studied the variation of vertical structure of precipitation (in
99 terms of occurrence and intensity) with SST and the differences in the vertical structure over
100 AS and BOB. On the other hand, information on the vertical structure of precipitation is
101 essential for improving the accuracy of rainfall estimation (Fu and Liu 2001; Sunilkumar et
102 al. 2015), understanding the dynamical and microphysical processes of hydrometeor
103 growth/decay mechanisms (Houze 2004; Greets and Dejene 2005; Saikranthi et al. 2014; Rao
104 et al. 2016) and for improving the latent heating retrievals (Tao et al. 2006, 2016). SST being
105 the main driving force to trigger precipitating systems through air-sea interactions (Sabin et
106 al. 2012; Nuijens et al. 2017), can alter the vertical structure of precipitation (Oueslati and
107 Bellon 2015). Therefore, the present study aims to understand the variation of vertical
108 structure of precipitation (in terms of precipitation top height and intensity) with SST over the
109 AS and BOB. Besides the SST, vertical structure can be modified by aerosols (or CCN,
110 mostly at the cloud formation stage) and thermodynamics of the ambient atmosphere. For
111 instance, recent studies have shown the impact of surface PM_{10} aerosols in altering the

112 vertical structure of precipitation (Guo et al., 2018). All these parameters, therefore, are
113 considered in the present study to explain the differences in the vertical structure.

114 **2. Data**

115 The present study utilizes 16 years (1998-2013) of TRMM-PR's 2A25 (version 7)
116 dataset, comprising of vertical profiles of attenuation corrected reflectivity (Iguchi et al.
117 2009), during the ISM. The range resolution of TRMM-PR reflectivity profiles is 250 m with
118 a horizontal footprint size of ~4.3 and 5 km before and after the boosting of its orbit from 350
119 km to 403 km, respectively. It scans $\pm 17^\circ$ from nadir with a beam width of 0.71° covering a
120 swath of 215 km (245 km after the boost). The uniqueness of TRMM-PR data is its ability in
121 pigeonholing the precipitating systems into convective, stratiform and shallow rain. This
122 classification is based on two methods namely the horizontal method (H - method) and the
123 vertical method (V - method) (Awaka et al. 2009). The original TRMM-PR 2A25 vertical
124 profiles of attenuation corrected reflectivity are gridded to a three dimensional Cartesian
125 coordinate system with a spatial resolution of $0.05^\circ \times 0.05^\circ$. The detailed methodology of
126 interpolating the TRMM-PR reflectivity data into the 3D Cartesian grid is discussed in Houze
127 et al. (2007). This dataset is available at the University of Washington website
128 (<http://trmm.atmos.washington.edu/>). Profiles are classified as deep (shallow), if their storm
129 top reflectivity ≥ 17 dBZ lies above (1 km below) the 0°C isotherm.

130 To understand the observed variations in the vertical structure of precipitation in the
131 light of microphysics of clouds, Moderate Resolution Imaging Spectroradiometer (MODIS)
132 AQUA satellite level 3 data (MYD08) are considered. In particular, the daily atmospheric
133 products of aerosol optical depth (AOD) (Hubanks et al. 2008) and cloud effective radius
134 (CER) liquid (Platnick et al. 2017) during the period 2003 and 2013 have been used. MODIS
135 AOD dataset is a collection of aerosol optical properties at 550 nm wavelength, as well as
136 particle size information. Level 2 MODIS AOD is derived from radiances using either one of

137 the three different algorithms, i.e., over ocean Remer et al. (2005) algorithm, over land the
 138 Dark-Target (Levy et al. 2007) algorithm and for brighter land surfaces the Deep-Blue (Hsu
 139 et al. 2004) algorithm. CER is nothing but the weighted mean of the size distribution of cloud
 140 drops i.e., the ratio of third moment to second moment of the drop size distribution. In the
 141 level 3 MODIS daily dataset, aerosol and cloud products of level 2 data pixels with valid
 142 retrievals within a calendar day are first aggregated and gridded to a daily average with a
 143 spatial resolution of $1^\circ \times 1^\circ$. For CER grid box values, CER values are weighted by the
 144 respective ice/liquid water cloud pixel counts for the spatiotemporal aggregation and
 145 averaging processes.

146 The background atmospheric structure (winds and total column water) and SST
 147 information are taken from the European Centre for Medium Range Weather Forecasting
 148 (ECMWF) Interim Reanalysis (ERA) (Dee et al. 2011). ERA-Interim runs 4DVAR
 149 assimilation twice daily (00 and 12 UTC) to determine the most likely state of the atmosphere
 150 at a given time (analysis). The consistency across variables in space and time (during 12-hour
 151 intervals) is thus ensured by the atmospheric model and its error characteristics as specified in
 152 the assimilation. ERA-Interim is produced at T255 spectral resolution (about 0.75° , ~ 83 km)
 153 with a temporal resolution of 6h for upper air fields and 3h for surface fields. The original
 154 $0.75^\circ \times 0.75^\circ$ spatial resolution gridded dataset is rescaled to a resolution of $0.125^\circ \times 0.125^\circ$.
 155 The temporal resolution of the dataset used in the present study is 6h (00, 06, 12 and 18
 156 UTC). The equivalent potential temperature (θ_e) is estimated from the ERA-Interim datasets
 157 using the following formula (Wallace and Hobbs 2006):

$$\theta_e = \theta \exp\left(\frac{L_v w_s}{C_p T}\right) \quad (1)$$

158 where θ is the potential temperature, L_v is the latent heat of vaporization, w_s is the saturation
 159 mixing ratio, C_p is the specific heat at constant pressure and T is the absolute temperature.

160 The variation of vertical structure of precipitation with SST are studied by considering
161 the dataset between 63 °E – 72 °E and 8 °N – 20 °N over the AS and 83 °E – 92 °E and 8 °N
162 – 21 °N over the BOB. These regions of interest along with the ISM seasonal mean SST over
163 the two seas are depicted in Fig. 1. These regions are selected in such a way that the costal
164 influence on SST is eluded from the analysis. As the rainfall is scanty over the western AS
165 (west of 63°E latitude) during the ISM (Saikranthi et al. 2018), this region is also not
166 considered in the present analysis. The seasonal mean SST is higher over the BOB than in the
167 AS by more than 1 °C during the ISM season, in agreement with Shenoi et al. (2002). The
168 nearest space and time matched SST data from ERA-Interim are assigned to the TRMM-PR
169 and MODIS observations for further analysis.

170 **3. Variation of vertical structure of precipitation with SST**

171 The occurrence (in terms of %) of conditional precipitation echoes ($Z \geq 17$ dBZ) at
172 different altitudes as a function of SST over the AS and the BOB is shown in Fig. 2. The
173 variation of precipitation echo occurrence frequency with SST is quite different over both the
174 seas. The top of the precipitation echoes extends to higher altitudes with increasing SST over
175 the AS, while such variation is not quite evident over the BOB. Precipitation echoes are
176 confined to < 8 km at lower SST (< 28 °C) over the AS, but exhibits a gradual rise in height
177 with increase in SST. Large population density of precipitation echoes at lower altitudes is
178 mainly due to the abundant occurrence of shallow storms over the AS (Saikranthi et al. 2014,
179 2019; Rao et al. 2016). Interestingly, the occurrence of precipitation echoes is seen at higher
180 altitudes even at lower SSTs over the BOB, indicating the presence of deeper storms. Such
181 systems exist at all SST's over the BOB.

182 To examine the variation of reflectivity profiles with SST, median profiles of
183 reflectivity in each SST bin are computed over the AS and the BOB separately for deep and
184 shallow systems and are depicted in Figs. 3 & 4, respectively. The space- and time-matched

185 conditional reflectivity profiles are grouped into 1°C SST bins and then the median is
186 estimated at each height, only if the number of conditional reflectivity pixels (Figs. 3c; 3f; 4c
187 & 4f) is greater than 500. The median reflectivity profiles corresponding to the deep systems
188 are distinctly different over the AS and the BOB (Figs. 3a & 3d), even at the same SST. Over
189 the AS, reflectivity of deep systems at different SSTs shows small variations (≤ 1 dBZ) above
190 the melting region (> 5 km), but varies significantly (~ 4.5 dBZ) below the melting level (< 5
191 km). These variations in reflectivity profiles with SST are negligible (< 0.5 dBZ) over the
192 BOB both above and below the melting region. The reflectivity increases from ~ 26.5 dBZ to
193 ~ 31 dBZ, with increase in SST from 26°C to 30°C over the AS, but it is almost the same (\sim
194 30 dBZ) at all SST's over the BOB below the melting layer. The standard deviation of
195 reflectivity, representing the variability in reflectivity within the SST bin, is similar at all
196 SSTs over both the seas except for the 26°C SST over AS. At this SST, the standard
197 deviation is lesser by ~ 1 dBZ than that of other SSTs.

198 The median reflectivity profiles of shallow storms depicted in Figs. 4a & 4d also
199 show a gradual increase in reflectivity from 20 dBZ to ~ 22 dBZ as SST changes from 26°C
200 to 31°C at the precipitation top altitude over the AS and don't show any variation with SST
201 over the BOB. However at 1 km altitude, except at 26°C SST over the AS, the reflectivity
202 variation with SST is not substantial over both the seas. The standard deviation of reflectivity
203 profiles show ~ 1 dBZ variation with SST (from 26°C to 31°C) at all altitudes over the AS
204 and don't show any variation over the BOB. The standard deviation of reflectivity for
205 shallow storms varies from 3 to 4 dBZ at the precipitation top altitude and 4.5 to 5.3 dBZ at 1
206 km altitude over the AS while it shows ~ 4 dBZ at precipitation top and ~ 5.5 dBZ at 1 km
207 altitude over the BOB.

208 **4. Factors affecting the vertical structure of precipitation and their variability with SST**

209 The formation and evolution of precipitating systems over oceans depend on
 210 dynamical, thermodynamical and microphysical factors, like SST, wind shear, vertical wind
 211 velocity, stability, CER, etc., and need to be considered for understanding the vertical
 212 structure of precipitation (Li and Min 2010; Creamean et al. 2013; Chen et al. 2015; Shige
 213 and Kummerow 2016; Guo et al 2018).

214 **4.1. Dynamical and thermodynamical factors:**

215 Takahashi and Dado (2018) have shown that zonal wind variations can also explain
 216 some variability of rain. To examine the impact of zonal wind on rainfall over the Arabian
 217 Sea and Bay of Bengal, the data are segregated into 3 wind regimes as weak (monsoon
 218 westerlies lies between 0 and 6 m s⁻¹), moderate (monsoon westerlies lies between 6 to 12 m
 219 s⁻¹) and strong (monsoon westerlies > 12 m s⁻¹) winds. The median vertical profiles of
 220 reflectivity are computed for each SST bin corresponding to deep and shallow systems (not
 221 shown here). Two important observations are noted from these figures. 1) Vertical profiles of
 222 reflectivity show considerable variation (2-5 dBZ) in all wind categories over the Arabian
 223 Sea, but such variations are absent over the Bay of Bengal. It implies that the reported
 224 differences in reflectivity profiles over the Arabian Sea and Bay of Bengal exist in all wind
 225 regimes. 2) The variation in reflectivity with SST increases with weak to strong wind regime
 226 over the Arabian Sea, indicating some influence of wind on reflectivity (rainfall) variation.

227 To understand the role of stability/instability, θ_e values computed from (1) using the
 228 ERA-Interim datasets during the ISM period over the AS and the BOB are averaged for a
 229 season and are depicted in Figs. 5(a) & 5(b), respectively. The surface θ_e (at 1000 hPa) values
 230 are larger over the BOB than those over AS for the same SST, indicating that the instability
 231 and convective available potential energy (CAPE) could be higher over the BOB. Indeed,
 232 higher CAPE is seen over the BOB (Fig. S1, calculated following Emanuel 1994) than AS at
 233 all SSTs by a magnitude > 300 J kg⁻¹. The θ_e increases with SST from 358 °K to 368 °K

234 from 27 °C to 31 °C and from 350 °K to 363 °K from 26 °C to 31 °C over the BOB and the
235 AS, respectively. The CAPE also increases with rise in SST over both the seas. To know the
236 stability of the atmosphere θ_e gradients are considered. Irrespective of SST, positive gradients
237 in θ_e are observed between 900 and 800 hPa levels over the AS indicating the presence of
238 strong stable layers. The strength of these stable layers decreases with increasing SST. These
239 stable layers are formed mainly due to the flow of continental dry warm air from Arabian
240 Desert and Africa above the maritime air causing temperature inversions below 750 hPa level
241 over the AS during the ISM period (Narayanan and Rao 1981). However over the BOB, such
242 temperature inversions are not seen in the lower troposphere.

243 To understand the effect of wind field on the vertical structure of precipitation,
244 profiles of ISM seasonal mean vertical wind velocity and vertical shear in horizontal wind at
245 various SSTs over the AS and the BOB are shown in Figs. 5(c), 5(d) & 5(e), 5(f)
246 respectively. The updrafts are prevalent at all SSTs throughout the troposphere over the BOB,
247 whereas downdrafts are seen in the mid-troposphere (between 200 and 600 hPa levels) up to
248 27 °C and updrafts in the entire troposphere at higher SSTs over the AS. Also, the magnitude
249 of the vertical wind velocity varies significantly with SST in the mid-troposphere over the
250 AS. Over the BOB, the magnitude of updrafts increases with altitude in the lower and middle
251 troposphere, but doesn't vary much with SST. In the mid-troposphere, updrafts are stronger
252 by $> 0.02 \text{ Pa s}^{-1}$ over the BOB than over the AS. The profiles shown in Fig. 5(e) & 5(f) are
253 the mean vertical shear in horizontal wind estimated following Chen et al. (2015) at different
254 levels with reference to 950 hPa level. The wind shear increases with increasing altitude at all
255 the SSTs up to 400 hPa, but the rate of increase is distinctly different between the AS and the
256 BOB at SSTs less than 28 °C and nearly the same at higher SSTs. The wind shear decreases
257 systematically with SST ($\sim 1.5 \text{ m s}^{-1}$ for 1° increase in SST) in the middle troposphere over
258 the AS while the change is minimal over the BOB ($\sim 2 \text{ m s}^{-1}$ for 27 °C and 31 °C).

259 Chen et al. (2015) highlighted the importance of mid-tropospheric wind shear in
260 generating mesoscale local circulations, like low-level cyclonic and upper-level anticyclonic
261 circulations. This feature is apparent over the AS, where down drafts are prevalent in mid-
262 upper troposphere and updrafts in the lower troposphere at lower SSTs. As SST increases, the
263 wind shear decreases and the updraft increases in the mid-troposphere. However, over the
264 BOB the wind shear is relatively weak when compared to the AS and hence the updrafts are
265 seen up to 200 hPa level at all SSTs. The weaker CAPE and stable mid-troposphere coupled
266 with upper- to mid- tropospheric downdrafts at lower SSTs over the AS inhibit the growth of
267 precipitating systems to higher altitudes and in turn precipitate in the form of shallow rain.
268 This result is in accordance with the findings of Shige and Kummerow (2016) that showed
269 the static stability at lower levels inhibits the growth of clouds and promotes the detrainment
270 of clouds over the Asian monsoon region and is considered as an important parameter in
271 determining the precipitation top height. As SST increases large CAPE and updrafts in the
272 middle troposphere collectively support the precipitating systems to grow to higher altitudes,
273 as evidenced in Fig. 2a. On the other hand, large CAPE and updrafts in the middle
274 troposphere prevalent over the BOB at all SSTs are conducive for the precipitating systems to
275 grow to higher altitudes as seen in Fig. 2b.

276 **4.2. Microphysical factors**

277 The observed differences in reflectivity profiles of precipitation with SST could be
278 originated at the cloud formation stage itself or manifested during the evolution stage or due
279 to both. Information on AOD and CER would be ideal to infer microphysical processes at the
280 cloud formation stage. CER values are mainly controlled by the ambient aerosols
281 concentration and the available moisture (Twomey 1977; Albrecht 1989; Tao et al. 2012; and
282 Rosenfeld et al. 2014). For fixed liquid water content, as the concentration of aerosols
283 increases, the number of cloud drops increases and CER decreases (Twomey 1977). To

284 understand the variation of AOD and total column water (TCW) and the resultant CER with
285 SST, the mean AOD and TCW for different SST bins are plotted in Figs. 6a & 6b. The mean
286 and standard error are calculated only when the number of data points is more than 100 in
287 each SST bin. AOD decreases from 0.62 to 0.31 with rise in SST from 26 °C to 31 °C over
288 the AS but only from 0.42 to 0.36 as SST varies from 27 °C to 30 °C and then increases at
289 higher SSTs over the BOB. The variation of TCW with SST (Fig. 6b) shows a gradual
290 increase with SST over the AS while it decreases initially from 27°C to 28°C, and then
291 increases over the BOB. At a given SST the TCW is more in the BOB (> 8 mm) than in the
292 AS.

293 The decrease in AOD and an increase in TCW with SST result in an increase in CER
294 (14.7 μm to 20.8 μm from 26°C to 31°C) over the AS (Fig. 7). On the other hand, CER
295 doesn't show much variation with SST (18.5 μm to 19.5 μm from 27°C to 31°C) over BOB
296 due to smaller variations in AOD and TCW. This also shows that the cloud droplets are
297 smaller in size at lower SSTs over the AS than BOB, while they are bigger and nearly equal
298 in size at higher SSTs. Since, reflectivity is more sensitive to the precipitating particle size (Z
299 $\propto D^6$), the smaller-sized hydrometeors at lower SSTs over the AS yield weaker reflectivity
300 than over the BOB (both for deep and shallow systems). As the SST increases, CER as well
301 as the reflectivity increases over the AS. At higher SSTs, the CER values are approximately
302 equal over both the seas and in turn the observed reflectivities (Figs. 3a & 4a). This suggests
303 that the variations seen in the reflectivity are originated in the cloud formation stage itself.

304 The hydrometeors also evolve during their descent to the ground due to several
305 microphysical processes. These processes can be inferred from the vertical structure of
306 precipitation or vertical profiles of reflectivity. The median reflectivity profiles of deep
307 systems show a gradual increase from ~ 10 km to 6 km and an abrupt enhancement is seen
308 just below 6 km over both the seas (Figs. 3a & 3d). The sudden enhancement at the freezing

309 level (radar bright band) is primarily due to the aggregation of hydrometeors, change in
310 dielectric factor from ice to water and change in fall speed from ice hydrometers to raindrops
311 (Fabry and Zawadzki 1995; Rao et al. 2008; Cao et al. 2013). Below the bright band,
312 raindrops grow by collision-coalescence process and reduce their size by either breakup
313 and/or evaporation processes. The collision-coalescence results in negative slope in the
314 reflectivity profile, whereas breakup and evaporation results in positive slope (Liu and Zipser
315 2013; Cao et al. 2013; Saikranthi et al. 2014; Rao et al. 2016). The observed negative slope
316 ($\sim -0.3 \text{ dBZ km}^{-1}$) in the median reflectivity profiles below the bright band indicates
317 dominance of low-level hydrometeor growth over both the seas. The magnitude of the slope
318 decreases with SST over the AS, while it is nearly equal at all SSTs over the BOB. It
319 indicates the growth rate decreases with SST over the AS and remains the same at all SSTs
320 over the BOB. The median reflectivity profiles of shallow systems also show negative slopes
321 ($\sim -1 \text{ dBZ km}^{-1}$) at all SSTs representing the predominance of low-level hydrometeor growth
322 by collision-coalescence processes over both the seas.

323 The present analysis shows that the observed reflectivity changes with SST over both
324 the seas originate at the cloud formation stage and magnify further during the descent of
325 hydrometeors to ground.

326 **5. Conclusions**

327 Sixteen years of TRMM-PR 2A25 reflectivity profiles and 11 years of MODIS AOD
328 and CER data are utilized to understand the differences in variation of vertical structure of
329 precipitation with SST over AS and BOB. Precipitation top height increases with SST over
330 the AS indicating that systems grow to higher altitudes with increase in SST while it is almost
331 same at all SSTs representing that the systems are deeper over the BOB. The decrease in
332 stability and mid-tropospheric wind shear with SST over the AS favour the formation of
333 deeper system at higher systems. However the low stability and small wind shear at all SSTs

334 over the BOB help the formation of deeper systems. The variation of reflectivity with SST is
335 found to be remarkable over the AS and marginal over the BOB. The reflectivity increases
336 with rise in SST over the AS and remains the same at all SSTs over the BOB. This change in
337 reflectivity over the AS is more prominent below the freezing level height (~ 4 dBZ) than the
338 above (~ 1 dBZ). Over the AS, the abundance of aerosols and less moisture at SSTs $< 27^\circ\text{C}$
339 result in high concentration of smaller cloud droplets. As SST increases the aerosol
340 concentration decreases and moisture increases leading to the formation of bigger cloud
341 droplets. Thus, the reflectivity increases with rise in SST over the AS. On the other hand,
342 AOD, TCW and CER do not show substantial variation with SST over the BOB and hence
343 the change in reflectivity is small. Over the BOB, the mid troposphere is wet and
344 hydrometeor's size at the formation stage is nearly the same at all SSTs. The evolution of
345 hydrometeors during their descent is also similar at all SST's. The collision-coalescence
346 process is predominant below the bright band region over both the seas and is responsible for
347 the observed negative slope in the reflectivity profiles.

348 **Acknowledgements**

349 The authors would like to thank Prof. Robert Houze and his team for the interpolated 3D
350 gridded TRMM-PR dataset (<http://trmm.atmos.washington.edu>), ECMWF (<http://data-portal.ecmwf.int/>) team for providing the ERA-Interim dataset and MODIS
351 (<https://ladsweb.modaps.eosdis.nasa.gov/>) science team for providing the AOD and CER
352 dataset. The authors express their gratitude to Prof. J. Srinivasan for his fruitful discussions
353 and valuable suggestions in improving the quality of the manuscript. The corresponding
354 author would like to thank Department of Science & Technology (DST), India for providing
355 the financial support through the reference number DST/INSPIRE/04/2017/001185. We
356 thank the anonymous referees for their critical comments in improving the quality of the
357 manuscript.
358

359
360
361
362
363
364
365
366
367
368
369
370
371
372
373
374
375
376
377
378
379
380
381
382
383
384

References

- Albrecht, B.A.: Aerosols, cloud microphysics, and fractional cloudiness, *Science*, 245, 1227–1230, 1989.
- Awaka, J., Iguchi, T., and Okamoto, K.: TRMM PR standard algorithm 2A23 and its performance on bright band detection, *J. Meteorol. Soc. Jpn.*, 87A, 31–52, 2009.
- Bhat, G. S., Gadgil, S., Kumar, P. V. H., Kalsi, S. R., Madhusoodanan, P., Murty, V. S., Rao, C. V. P., Babu, V. R., Rao, L.V., Rao, R. R., Ravichandran, M., Reddy, K.G., Rao, P. S., Sengupta, D., Sikka, D. R., Swain, J., and Vinayachandran, P. N.: BOBMEX: The Bay of Bengal Monsoon Experiment, *Bull. Amer. Meteor. Soc.*, 82, 2217–2244, 2001.
- Cao, Q., Hong, Y., Gourley, J. J., Qi, Y., Zhang, J., Wen, Y., and Kirstetter, P. E.: Statistical and physical analysis of the vertical structure of precipitation in the mountainous west region of the United States using 11+ years of space borne observations from TRMM precipitation radar, *J. Appl. Meteorol. Climatol.*, 52, 408-424, 2013.
- Chaudhari, H. S., Pokhrel, S., Kulkarni, A., Hazra, A., and Saha, S. K.: Clouds-SST relationship and interannual variability modes of Indian summer monsoon in the context of clouds and SSTs: observational and modelling aspects, *Int. J. Climatol.*, doi:10.1002/joc.4664, 2016.
- Chaudhari, H. S., Pokhrel, S., Mohanty, S., and Saha, S. K.: Seasonal prediction of Indian summer monsoon in NCEP coupled and uncoupled model, *Theor. Appl. Climatol.*, 114, 459–477, doi:10.1007/s00704-013-0854-8, 2013.
- Chen, Q., Fan, J., Hagos, S., Gustafson Jr., W. I., and Berg, L. K.: Roles of wind shear at different vertical levels: Cloud system organization and properties, *J. Geophys. Res. Atmos.*, 120, 6551–6574, 2015.
- Creamean, J. M., Suski, K. J., Rosenfeld, D., Cazorla, A., DeMott, P. J., Sullivan, R. C., White, A. B., Ralph, F. M., Minnis, P., Comstock, J. M., Tomlinson, J. M., Kimberly

- 385 A., and Prather, K. A.: Dust and biological aerosols from the Sahara and Asia influence
386 precipitation in the western U.S., *Science*, 339, 1572–1578,
387 doi:10.1126/science.1227279, 2013.
- 388 Dee, D. P., et al.: The ERA-Interim reanalysis: Configuration and performance of the data
389 assimilation system, *Q. J. R. Meteorol. Soc.*, 137, 553–597, 2011.
- 390 Emanuel, K. A.: Atmospheric convection. Oxford University Press, Oxford, 1994.
- 391 Fabry, F., and Zawadzki, I.: Long-term radar observations of the melting layer of
392 precipitation and their interpretation, *J. Atmos. Sci.*, 52, 838–851, 1995.
- 393 Feng, X., Haines, K., Liu, C., de Boissésón, E., and Polo, I., Improved SST-precipitation
394 intraseasonal relationships in the ECMWF coupled climate reanalysis, *Geophys. Res.
395 Lett.*, 45, 3664–3672, 2018.
- 396 Findlater, J.: A major low-level air current near the Indian Ocean during the northern
397 summer, *Q. J. R. Meteorol. Soc.*, 95, 362–380, 1969.
- 398 Fu, Y., and Liu, G.: The variability of tropical precipitation profiles and its impact on
399 microwave brightness temperatures as inferred from TRMM data, *J. Appl. Meteorol.*,
400 40, 2130–2143, 2001.
- 401 Gadgil, S., Joseph, P. V., and Joshi, N. V.: Ocean atmosphere coupling over monsoonal
402 regions, *Nature*, 312, 141–143, 1984.
- 403 Gadgil, S.: Monsoon–ocean coupling. *Current Sci.*, 78, 309–323, 2000.
- 404 Geerts, B., and Dejene, T.: Regional and diurnal variability of the vertical structure of
405 precipitation systems in Africa based on space borne radar data, *J. Clim.*, 18, 893–916,
406 2005.
- 407 Guo, J., Liu, H., Li, Z., Rosenfeld, D., Jiang, M., Xu, W., Jiang, J. H., He, J., Chen, D., Min,
408 M., and Zhai, P.: Aerosol-induced changes in the vertical structure of precipitation: a
409 perspective of TRMM precipitation radar, *Atmos. Chem. Phys.*, 18, 13329–13343,

- 410 <https://doi.org/10.5194/acp-18-13329-2018>, 2018.
- 411 Houze, R. A., and Churchill, D. D.: Mesoscale organization and cloud microphysics in a Bay
412 of Bengal depression, *J. Atmos. Sci.*, 44, 1845–1867, 1987.
- 413 Houze, R. A., Rasmussen, K. L., Zuluaga, M. D., and Brodzik, S. R.: The variable nature of
414 convection in the tropics and subtropics: A legacy of 16 years of the Tropical rainfall
415 measuring mission satellite, *Rev. Geophys.*, 53, 994–1021, 2015.
- 416 Houze, R. A., Wilton, D. C., and Smull, B. F.: Monsoon convection in the Himalayan region
417 as seen by the TRMM precipitation radar, *Q. J. R. Meteorol. Soc.*, 133, 1389-1411,
418 2007.
- 419 Houze, R. A.: Mesoscale convective systems, *Rev. Geophys.*, 42, RG4003, doi:
420 10.1029/2004RG000150, 2004.
- 421 Hsu, N., Tsay, S., King, M., and Herman, J.: Aerosol properties over bright-reflecting source
422 regions, *Geosci. Remote Sens. IEEE Trans.*, 42, 557–569, 2004.
- 423 Hubanks, P., King, M., Platnick, S., and Pincus, R.: MODIS atmosphere L3 gridded product
424 algorithm theoretical basis document collection 005 Version 1.1, Tech. Rep. ATBD-
425 MOD-30, NASA, 2008.
- 426 Iguchi, T., Kozu, T., Kwiatkowski, J., Meneghini, R., Awaka, J., and Okamoto, K.:
427 Uncertainties in the rain profiling algorithm for the TRMM precipitation radar, *J.*
428 *Meteor. Soc. Japan*, 87A, 1–30, doi:10.2151/jmsj.87A.1, 2009.
- 429 Krishnamurti, T. N.: Summer monsoon experiment – A review. *Mon. Wea. Rev.*, 113, 1590-
430 1626, 1985.
- 431 Krishnamurti, T.: Cooling of the Arabian Sea and the onset-vortex during 1979. Recent
432 progress in equatorial oceanography: A report of the final meeting of SCOR
433 WORKING GROUP 47 in Venice, Italy, 1-12, 1981. [Available from Nova Univ.,
434 Ocean Science Center, Dania, FL 33004].

- 435 Kumar, S., Hazra, A., and Goswami, B. N.: Role of interaction between dynamics,
436 thermodynamics and cloud microphysics on summer monsoon precipitating clouds over
437 the Myanmar coast and the Western Ghats, *Clim. Dyn.*, 43, 911–924,
438 doi:10.1007/s00382-013-1909-3, 2014.
- 439 Levy, R., Remer, L., Mattoo, S., Vermote, E., and Kaufman, Y.: Second-generation
440 operational algorithm: Retrieval of aerosol properties over land from inversion of
441 moderate resolution imaging spectroradiometer spectral reflectance, *J. Geophys. Res.*,
442 112, D13, doi:10.1029/2006JD007811, 2007.
- 443 Li, R., and Min, Q.-L.: Impacts of mineral dust on the vertical structure of precipitation, *J.*
444 *Geophys. Res.*, 115, D09203, doi:10.1029/2009JD011925, 2010.
- 445 Liu, C., Zipser, E., and Nesbitt, S. W.: Global distribution of tropical deep convection:
446 Different perspectives using infrared and radar as the primary data source, *J. Climate*,
447 20, 489-503, 2007.
- 448 Liu, C., and Zipser, E. J.: Why does radar reflectivity tend to increase downward toward the
449 ocean surface, but decrease downward toward the land surface?, *J. Geophys. Res.*
450 *Atmos.*, 118, 135-148, doi: 10.1029/2012JD018134, 2013.
- 451 Meenu, S., Parameswaran, K., and Rajeev, K.: Role of sea surface temperature and wind
452 convergence in regulating convection over the tropical Indian Ocean, *J. Geophys. Res.*
453 *Atmos.*, 117, D14102, 2012.
- 454 Nair, A. K. M., and Rajeev, K.: Multiyear CloudSat and CALIPSO observations of the
455 dependence of cloud vertical distribution on sea surface temperature and tropospheric
456 dynamics, *J. Clim.*, 27, 672–683, doi:10.1175/JCLI-D-13-00062.1, 2014.
- 457 Narayanan, M. S., and Rao, B. M.: Detection of monsoon inversion by TIROS-N satellite,
458 *Nature*, 294, 546-548, 1981.
- 459 Nuijens, L., Emanuel, K., Masunaga, H., and L’Ecuyer, T.: Implications of warm rain in

- 460 shallow cumulus and congestus clouds for large-scale circulations, *Surv. Geophys.*, 38,
461 1257-1282, 2017.
- 462 Oueslati, B., and Bellon, G.: The double ITCZ bias in CMIP5 models: interaction between
463 SST, large-scale circulation and precipitation. *Clim. Dyn.*, 44, 585-607, 2015.
- 464 Platnick, S., et al.: The MODIS cloud optical and microphysical products: Collection 6
465 updates and examples from Terra and Aqua, *IEEE Trans. Geosci. Remote Sens.*, 55,
466 502–525, doi:10.1109/TGRS.2016.2610522, 2017.
- 467 Rajeevan, M., Unnikrishnan, C. K., and Preethi, B.: Evaluation of the ENSEMBLES multi-
468 model seasonal forecasts of Indian summer monsoon variability, *Clim. Dyn.*, 38, 2257–
469 2274, 2012.
- 470 Rajendran, K., Nanjundiah, R. S., Gadgil, S., and Srinivasan, J.: How good are the
471 simulations of tropical SST–rainfall relationship by IPCC AR4 atmospheric and
472 coupled models?, *J. Earth Sys. Sci.*, 121(3), 595–610, 2012.
- 473 Rajendran, K., Gadgil, S. and Surendran, S.: Monsoon season local control on precipitation
474 over warm tropical oceans, *Meteorol. Atmos. Phys.*, doi:10.1007/s00703-018-0649-7,
475 2018.
- 476 Rao, T. N., Kirankumar, N. V. P., Radhakrishna, B., Rao, D. N., and Nakamura, K.:
477 Classification of tropical precipitating systems using wind profiler spectral moments.
478 Part I: Algorithm description and validation, *J. Atmos. Oceanic Technol.*, 25, 884–897,
479 2008.
- 480 Rao, T. N., Saikranthi, K., Radhakrisna, B., and Rao, S. V. B.: Differences in the
481 climatological characteristics of precipitation between active and break spells of the
482 Indian summer monsoon, *J. Clim.*, 29, 7797-7814, 2016.

- 483 Remer, L., Kaufman, Y., Tanré, D., Mattoo, S., Chu, D., Martins, J., Li, R., Ichoku, C.,
484 Levy, R., Kleidman, R., Eck, T., Vermote, E., and Holben, B.: The MODIS aerosol
485 algorithm, products, and validation, *J. Atmos. Sci.*, 62, 947–973, 2005.
- 486 Romatschke, U., Medina, S., and Houze, R. A.: Regional, seasonal, and diurnal variations of
487 extreme convection in the South Asian region, *J. Clim.*, 23, 419–439, 2010.
- 488 Rosenfeld, D., et al.: Global observations of aerosol-cloud-precipitation-climate interactions,
489 *Rev. Geophys.*, 52, 750-808, doi:10.1002/2013RG000441, 2014.
- 490 Roxy, M., Tanimoto, Y., Preethi, B., Terray, P., and Krishnan, R.: Intraseasonal SST-
491 precipitation relationship and its spatial variability over the tropical summer monsoon
492 region, *Clim. Dyn.*, 41, 45-61, 2013.
- 493 Roxy, M.: Sensitivity of precipitation to sea surface temperature over the tropical summer
494 monsoon region—and its quantification, *Clim. Dyn.*, 43, 1159-1169, 2014.
- 495 Sabin, T., Babu, C., and Joseph, P.: SST–convection relation over tropical oceans, *Int. J.*
496 *Climatol.* 33, 1424–1435, 2012.
- 497 Saikranthi, K., Radhakrishna, B., Satheesh, S. K., and Rao, T. N.: Spatial variation of
498 different rain systems during El Niño and La Niña periods over India and adjoining
499 ocean, *Clim. Dyn.*, 50, 3671-3685, doi: 10.1007/s00382-017-3833-4, 2018.
- 500 Saikranthi, K., Rao, T. N., Radhakrishna, B., and Rao, S. V. B.: Morphology of the vertical
501 structure of precipitation over India and adjoining oceans based on long-term
502 measurements of TRMMPR, *J. Geophys. Res. Atmos.*, 119, 8433–8449, doi:
503 10.1002/2014JD021774, 2014.
- 504 Saikranthi, K., Radhakrishna, B., Rao, T. N., and Satheesh, S. K.: Differences in the
505 association of sea surface temperature - precipitating systems over the Bay of Bengal
506 and the Arabian Sea during southwest monsoon season. *Int. J. Climatol.*,
507 doi:10.1002/joc.6074, 2019.

- 508 Sathiyamoorthy, V., Mahesh, C., Gopalan, K., Prakash, S., Shukla, B. P., Mathur, A.:
509 Characteristics of low clouds over the Arabian Sea, *J. Geophys. Res. Atmos.*, 118,
510 13489-13503, 2013.
- 511 Schumacher, C. and Houze, R. A.: Stratiform rain in the tropics as seen by the TRMM
512 precipitation radar, *J. Climate.*, 16, 1739–1756, 2003.
- 513 Sengupta, D., Goswami, B. N., and Senan, R.: Coherent intraseasonal oscillations of ocean
514 and atmosphere during the Asian summer monsoon, *Geophys. Res. Lett.*, 28, 4127–
515 4130, 2001.
- 516 Shenoi, S. S. C., Shankar, D., and Shetye, S. R.: Differences in heat budgets of the near-
517 surface Arabian Sea and Bay of Bengal: Implications for the summer monsoon, *J.*
518 *Geophys. Res.*, 107(C6), 3052, doi:10.1029/2000JC000679, 2002.
- 519 Shige, S. and Kummerow, C.D.: Precipitation-Top Heights of Heavy Orographic Rainfall in
520 the Asian Monsoon Region, *J. Atmos. Sci.*, 73, 3009–3024, 2016.
- 521 Shige, S., Nakano, Y., and Yamamoto, M. K.: Role of orography, diurnal cycle, and
522 intraseasonal oscillation in summer monsoon rainfall over Western Ghats and Myanmar
523 coast, *J. Climate*, 30, 9365–9381, doi:10.1175/JCLI-D-16-0858.1, 2017.
- 524 Sunilkumar, K., Rao, T. N., Saikranthi, K., and Rao, M. P.: comprehensive evaluation of
525 multisatellite precipitation estimates over India using gridded rainfall data, *J. Geophys.*
526 *Res. Atmos.*, 120, doi:10.1002/2015JD023437, 2015.
- 527 Takahashi, H. G., and Dado, J. M. B.: Relationship between sea surface temperature and
528 rainfall in the Philippines during the Asian summer monsoon, *J. Meteor. Soc. Japan.*,
529 96 (3), 283–290, doi:10.2151/jmsj.2018-03, 2018.
- 530 Takayabu, Y. N., Shige, S., Tao, W., and Hirota, N.: Shallow and deep latent heating modes
531 over tropical Oceans observed with TRMM PR spectral latent heating Data, *J. Climate*,
532 23, 2030–2046, 2010.

- 533 Tao, W.-K., Chen, J.-P., Li, Z., Wang, C., and Zhang, C.: Impact of aerosols on convective
534 clouds and precipitation, *Rev. Geophys.*, 50, RG2001, doi:10.1029/2011RG000369,
535 2012.
- 536 Tao, W.-K., et al.: Retrieval of latent heating from TRMM measurements, *Bull. Am.*
537 *Meteorol. Soc.*, 87, 1555–1572, 2006.
- 538 Tao, W.-K., et al.: TRMM latent heating retrieval: Applications and comparisons with field
539 campaigns and large-scale analyses, *Meteorological Monographs - Multi-scale*
540 *Convection-Coupled Systems in the Tropics: A tribute to Dr. Michio Yanai*, 56, 2.1-
541 2.34, doi:10.1175/AMSMONOGRAPHS-D-15-0013.1, 2016.
- 542 Twomey, S.: The influence of pollution on the short wave albedo of clouds, *J. Atmos. Sci.*,
543 34, 1149–1152, 1977.
- 544 Wallace, J. M., and Hobbs, P. V.: Atmospheric science: An introductory survey, Second
545 edition, Academic press, pp. 85, 2006.
- 546 Wang, B., Ding, Q., Fu, X., Kang, I.-S., Jin, K., Shukla, J., and Doblas-Reyes, F.:
547 Fundamental challenge in simulation and prediction of summer monsoon rainfall,
548 *Geophys. Res. Lett.*, 32, L15711, doi:10.1029/2005GL022734, 2005.
- 549 Weller, R. A., Farrar, J. T., Buckley, J., Mathew, S., Venkatesan, R., Lekha, J. S., Chaudhuri,
550 D., Kumar, N. S., and Kumar, B. P.: Air-sea interaction in the Bay of Bengal,
551 *Oceanography*, 29(2), 28–37, 2016.
- 552 Woolnough, S.J., Slingo, J.M., and Hoskins, B.J.: The relationship between convection and
553 sea surface temperature on intraseasonal timescales, *J. Climate*, 13, 2086–2104, 2000.
- 554 Wu, R., and Kirtman, B. P.: Roles of Indian and Pacific Ocean air–sea coupling in tropical
555 atmospheric variability, *Clim. Dyn.*, 25(2–3), 155–170, 2005.
- 556
- 557

Figure captions

558
559
560
561
562
563
564
565
566
567
568
569
570
571
572
573
574
575
576
577
578
579
580
581
582
583

Figure 1: Spatial distribution of ISM mean SST (in °C) obtained from ERA-Interim reanalysis data over the AS (63°E-72°E & 8°N-20°N) and the BOB (83°E-92°E & 8°N-21°N). The regions considered in this analysis over these two seas are shown with the boxes.

Figure 2: (a) and (b) represent the altitudinal distribution of occurrence of conditional reflectivity (≥ 17 dBZ) as a function of SST with respect to precipitation occurrence at that particular SST interval over the AS and the BOB, respectively.

Figure 3: (a), (d) and (b), (e) represent vertical profiles of median reflectivity correspond to deep systems and their standard deviation (in dBZ) with SST over the AS and the BOB, respectively during the ISM season. (c) and (f) show the number of conditional reflectivity pixels at each altitude used for the estimation of the median and standard deviation.

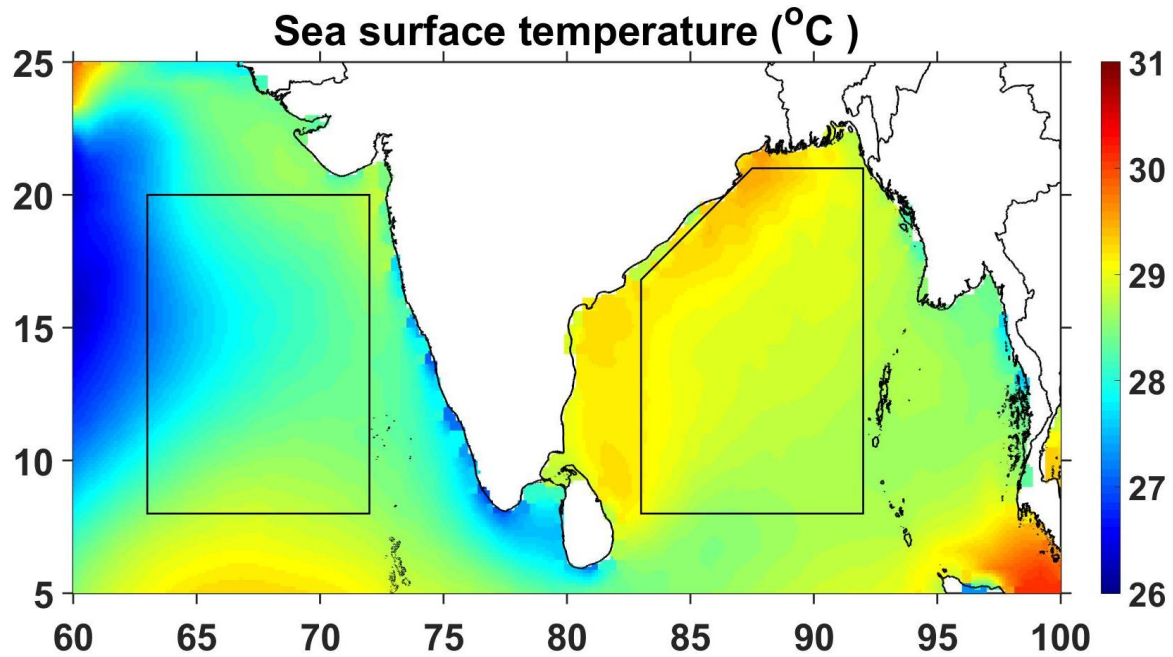
Figure 4: Same as Fig. 3 but for shallow precipitating systems.

Figure 5: (a) and (b), respectively, represent the vertical profiles of mean θ_e (in K) with SST over the AS and the BOB during the ISM season. (c) and (d) and (e) and (f) are same as (a) and (b) but for mean vertical velocity (in Pa s^{-1}) and wind gradient with reference to 950 hPa level (in m s^{-1}).

Figure 6: (a) Mean and standard error of AOD and (b) TCW (in kg m^{-2}) with SST over the AS and the BOB during ISM.

Figure 7: Variation of mean and standard error of CER liquid (in μm) with SST over the AS and the BOB during the ISM season.

Figures



586

587 **Figure 1:** Spatial distribution of ISM mean SST (in °C) obtained from ERA-Interim
588 reanalysis data over the AS (63°E-72°E & 8°N-20°N) and the BOB (83°E-92°E &
589 8°N-21°N). The regions considered in this analysis over these two seas are shown
590 with the boxes.

591

592

593

594

595

596

597

598

599

600

601

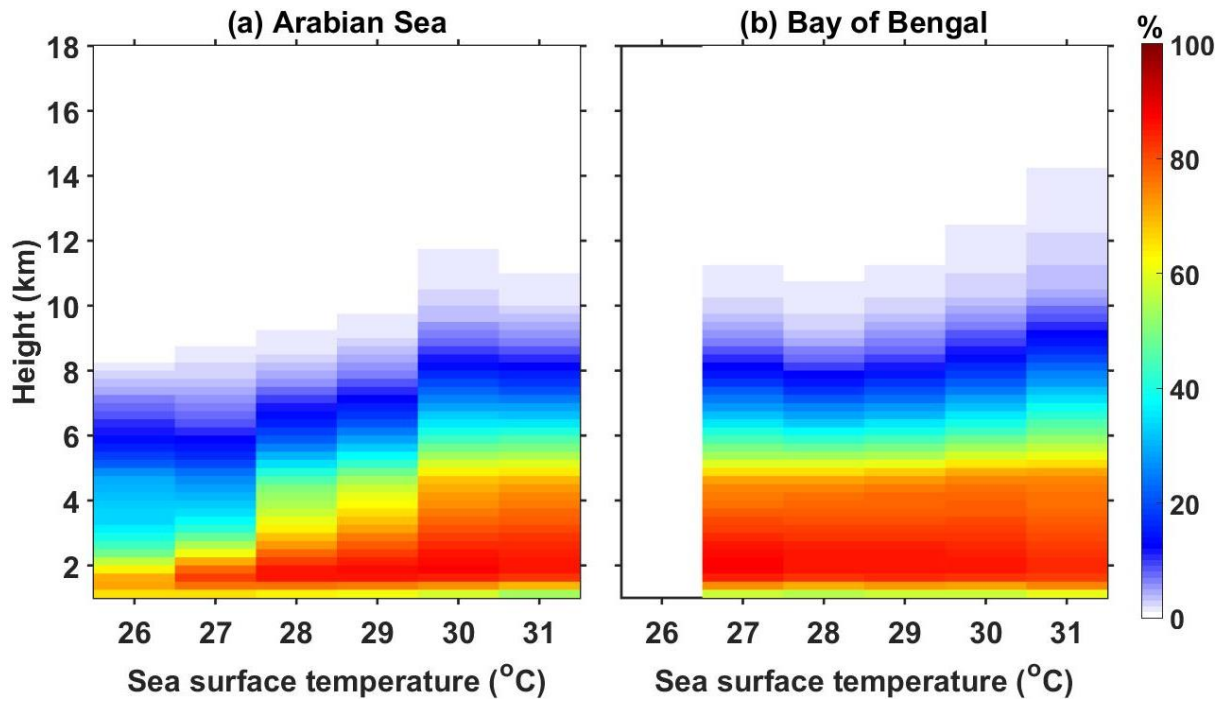
602

603

604

605

606



607

608

609 **Figure 2:** (a) and (b) represent the altitudinal distribution of occurrence of conditional
 610 reflectivity (≥ 17 dBZ) as a function of SST with respect to precipitation occurrence at
 611 that particular SST interval over the AS and the BOB, respectively.

612

613

614

615

616

617

618

619

620

621

622

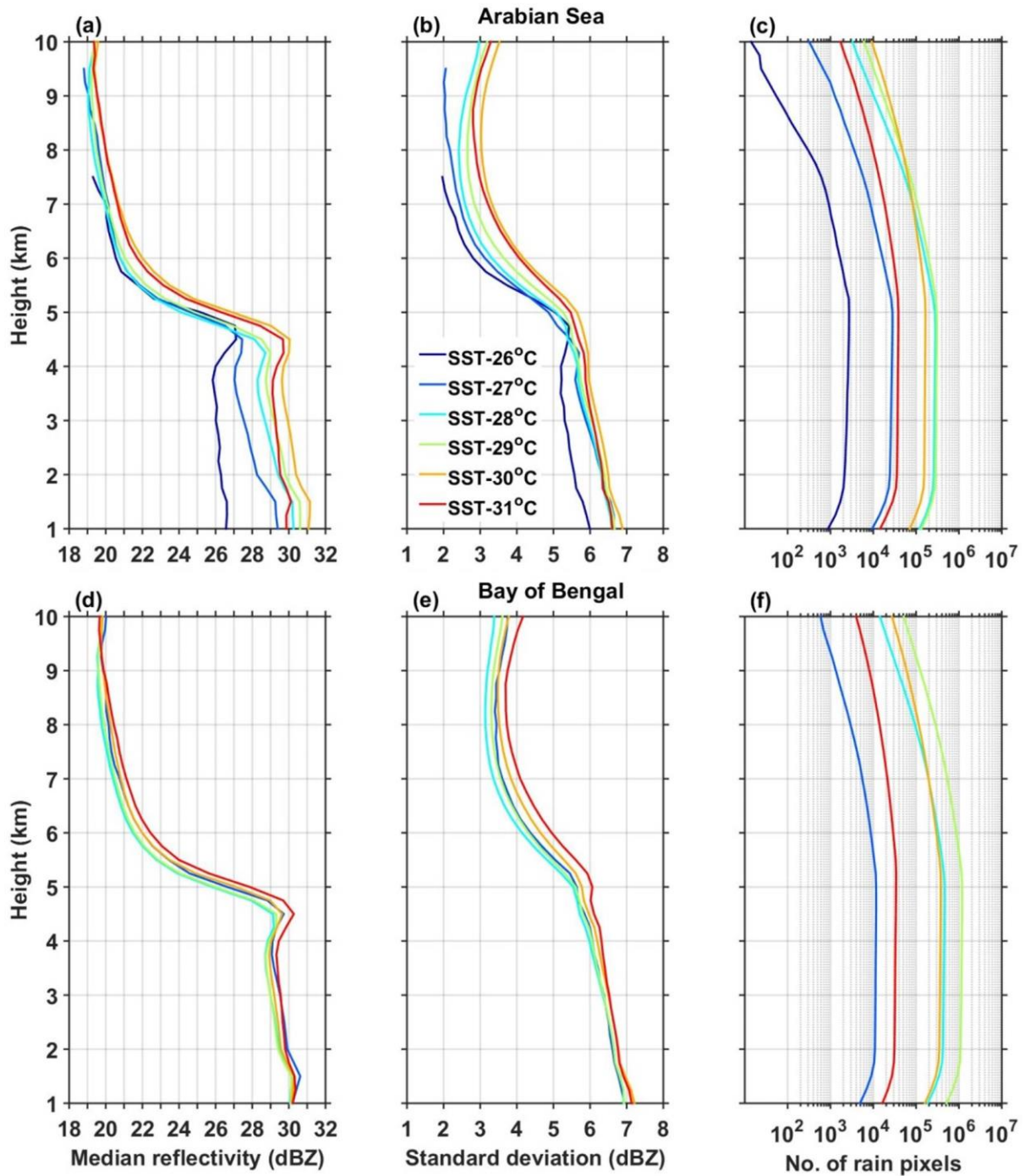
623

624

625

626

627



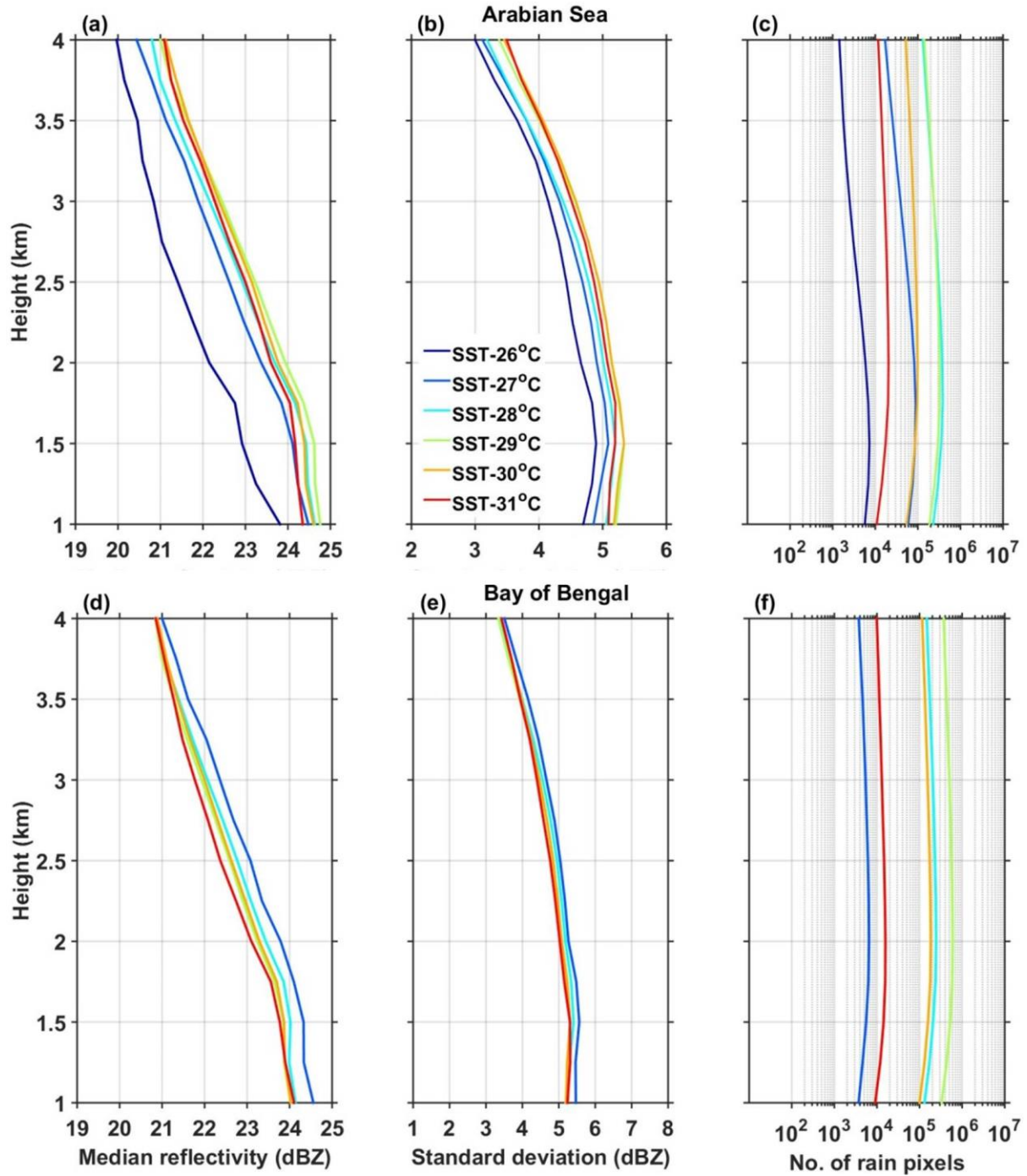
628

629 **Figure 3:** (a), (d) and (b), (e) represent vertical profiles of median reflectivity correspond to
 630 deep systems and their standard deviation (in dBZ) with SST over the AS and the
 631 BOB, respectively during the ISM season. (c) and (f) show the number of conditional
 632 reflectivity pixels at each altitude used for the estimation of the median and
 633 standard deviation.

634

635

636



637

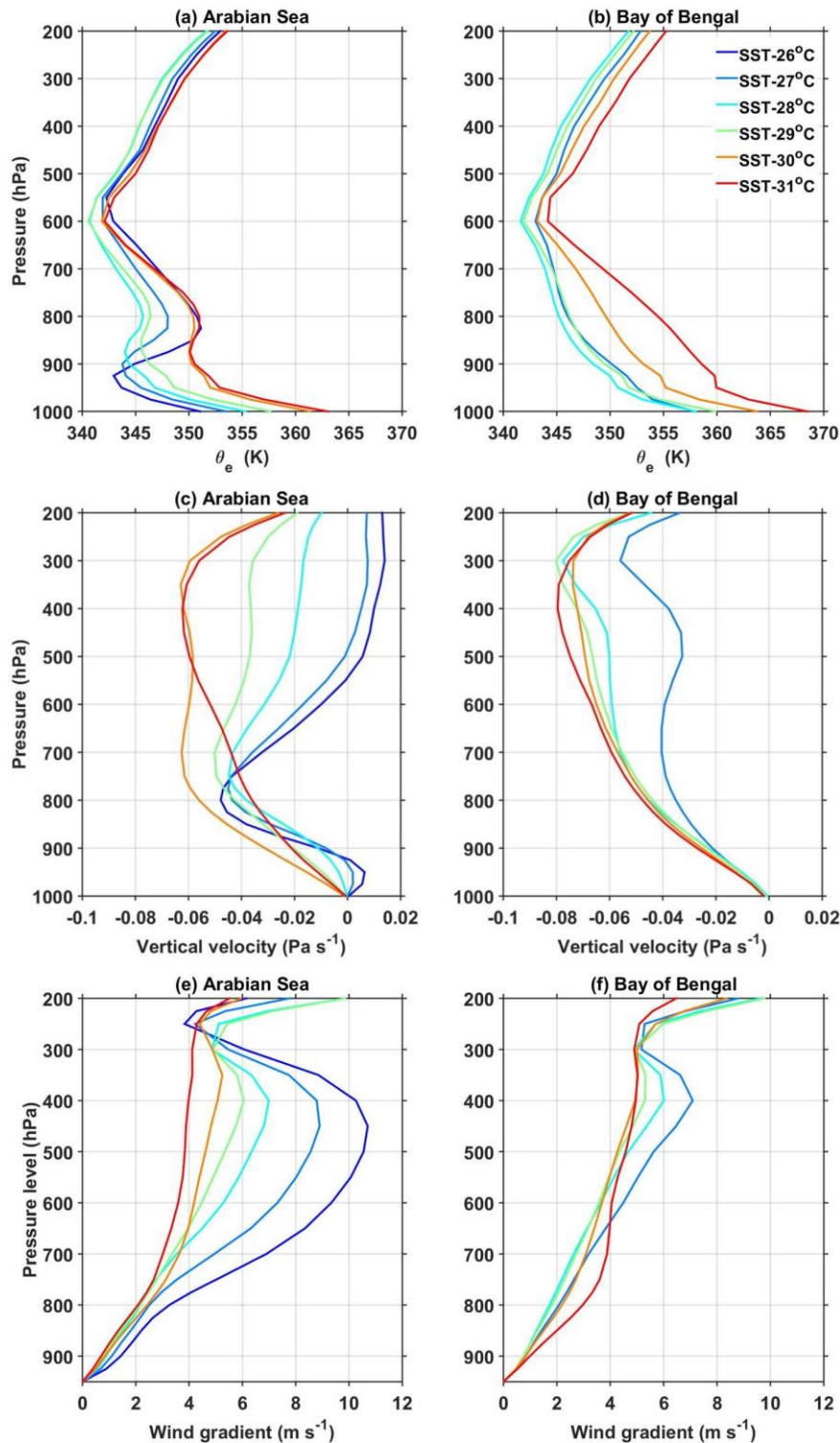
638 **Figure 4:** Same as Fig. 3 but for shallow precipitating systems.

639

640

641

642
 643
 644
 645
 646
 647
 648
 649
 650
 651
 652
 653
 654
 655
 656
 657
 658
 659
 660
 661
 662
 663
 664
 665
 666
 667
 668



669 **Figure 5:** (a) and (b), respectively, represent the vertical profiles of mean θ_e (in K) with SST
 670 over the AS and the BOB during the ISM season. (c) and (d) and (e) and (f) are same
 671 as (a) and (b) but for mean vertical velocity (in Pa s^{-1}) and wind gradient with
 672 reference to 950 hPa level (in m s^{-1}).

673
 674
 675
 676
 677
 678
 679
 680
 681
 682
 683
 684
 685
 686
 687
 688
 689
 690
 691
 692
 693
 694
 695
 696
 697
 698
 699
 700
 701
 702
 703

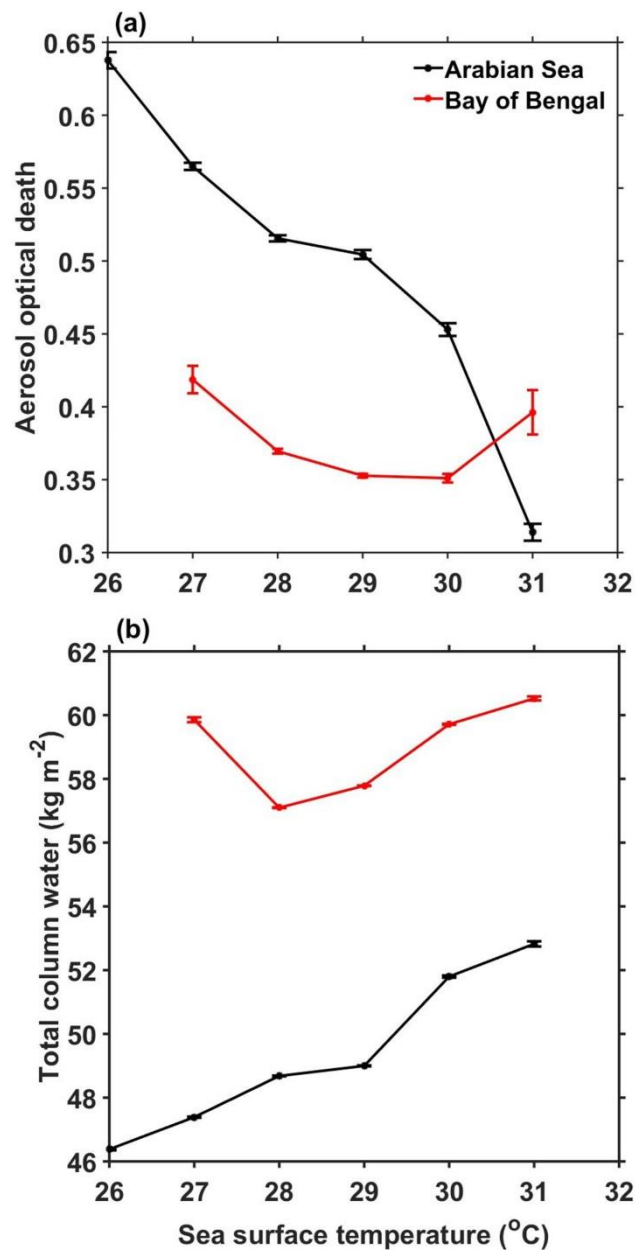


Figure 6: (a) Mean and standard error of AOD and (b) TCW (in kg m⁻²) with SST over the AS and the BOB during ISM.

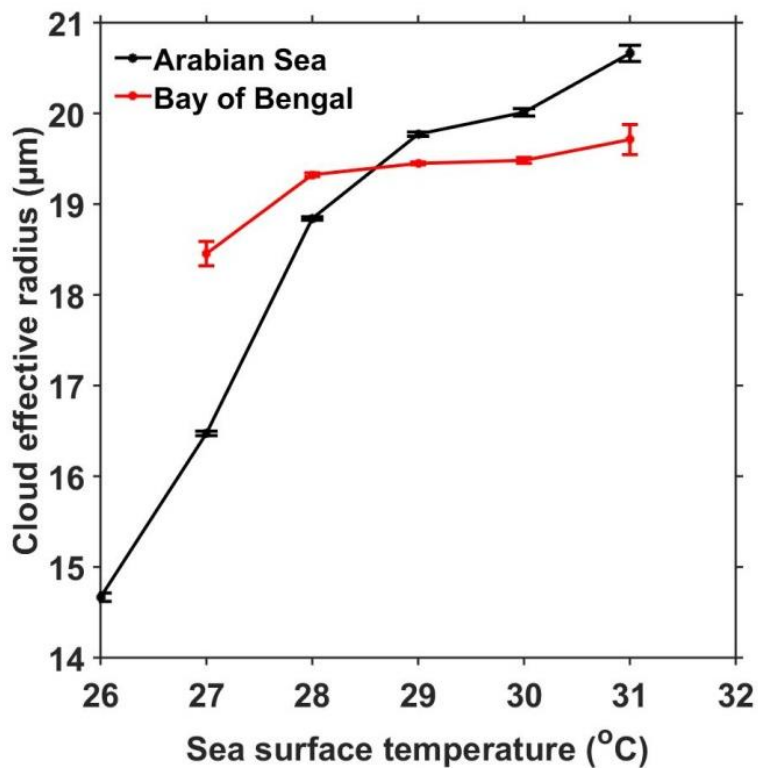


Figure 7: Variation of mean and standard error of CER liquid (in μm) with SST over the AS and the BOB during the ISM season.

Supplementary material

735
736 Satheesh et al. (2006) showed an increase in AOD with increase in latitude over the AS due
737 to the dust advection from Arabia desert regions during ISM season, whereas SST decreases
738 with increase in the latitude. In other words the SST is low and AOD is high in northern AS
739 whereas over the southern AS, SST is high and AOD is low. This contrasting spatial
740 distribution of AOD and SST could cause a negative correlation between AOD and SST as
741 depicted in Fig. 6a. To examine whether the observed decrease in AOD with increase in SST
742 over the AS is due to the latitudinal variation of AOD or exists at all latitudes, we have
743 segregated the data into 2° latitude bins and plotted the mean AOD with SST for all bins and
744 is depicted in Fig. S2. In spite of the magnitude, AOD variation with SST is nearly similar at
745 all latitudes of the AS, i.e., the higher AOD is observed at lower SSTs and vice versa (Fig.
746 S2a). On the other hand the latitudinal variation of AOD with SST over the BOB shown in
747 Fig. S2b also show a decrease in AOD with SST till 30 °C but the magnitude of variation is
748 trivial relative to the AS. Also, as depicted in Fig. 6a AOD increases above 30 °C with SST
749 over the BOB. This indicates that though there is a difference in magnitude of variation,
750 AOD varies with SST over both the seas at all latitudes. This analysis is repeated using the
751 multi-angle imaging spectroradiometer (MISR) dataset (which is not shown here) for small,
752 medium large aerosol particles. Interestingly all three types also show a decrease in AOD
753 with rise in SST over both the seas.

754
755 Satheesh, S. K., Moorthy, K. K., Kaufman, Y. J., and Takemura, T.: Aerosol Optical depth,
756 physical properties and radiative forcing over the Arabian Sea, *Meteorol. Atmos.*
757 *Phys.*, 91, 45–62, doi:10.1007/s00703-004-0097-4, 2006.

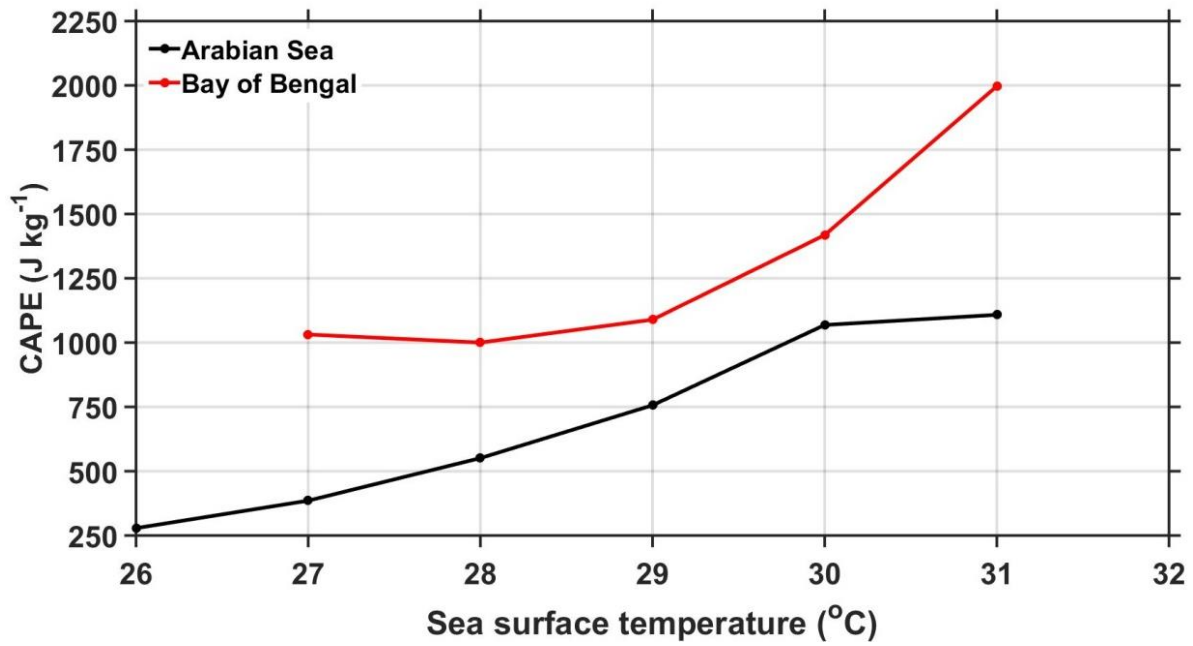
758

759

760

761

762



763

764 **Figure S1:** Variation of mean CAPE (in J kg⁻¹) with SST over the AS and the BOB during
765 the ISM season.

766

767

768

769

770

771

772

773

774

775

776

777

778

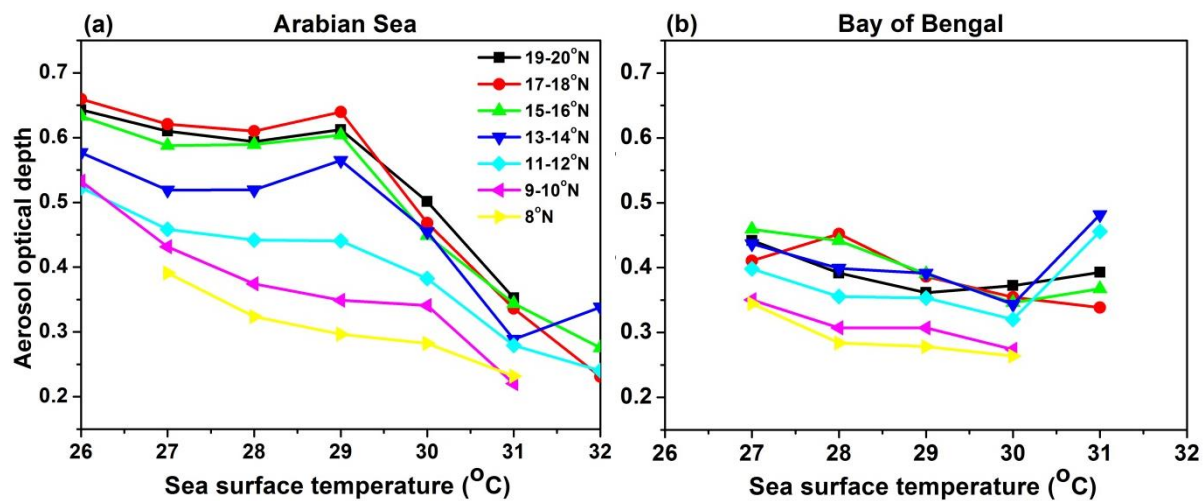
779

780

781

782

783



784

785 **Figure S2:** (a) and (b), respectively, represent latitudinal variation (for every 2° latitude
 786 interval) of mean AOD over the AS (between 63°E and 72°E) and the BOB (between
 787 83°E and 92°E).

788